Journal of Biomedical Optics

SPIEDigitalLibrary.org/jbo

Optical analysis of human eye using electromagnetic wave theory

Melih G. Can
Bilgehan B. Oner
Hamza Kurt

SPIE

Optical analysis of human eye using electromagnetic wave theory

Melih G. Can, Bilgehan B. Oner, and Hamza Kurt
TOBB University of Economics and Technology, Department of Electrical and Electronics Engineering, Nanophotonics Research Laboratory, Ankara 06560, Turkey

Abstract. We present a two-dimensional electromagnetic analysis of light propagation through the human eye to examine the eye's optical properties. The electromagnetic approach has intriguing advantages over the conventional and frequently implemented ray optics analysis. The chromatic, spherical, and coma aberrations and the intensity of the focused light at the retina are computed in this work via full-wave analysis. We also investigate the effects of the cornea's and lens's curved structures on the focusing mechanism. The focal length and chromatic and spherical aberrations are observed to change owing to age-related refractive index variation in the lens. In addition, the effects of the lens and curvatures of the human eye on focusing are analyzed. Consequently, for both young and old human eye lenses, the differences due to the aberration variations, curvature surfaces, and gradient index are explored by the wave approach. The intensity distributions on the retina for both on- and off-axis illumination are calculated. A strong correlation between the locations of the nerve fibers and the intensity distribution is confirmed. On the basis of the findings, we can conclude that visual impairment due to deterioration of the human eye structure is more dramatic than that due to aging.
[DOI: 10.1117/1.JBO.18.10.105006]

Keywords: human eye; aberration; electromagnetic wave analysis; numerical modeling.

Paper 130138RR received Mar. 11, 2013; revised manuscript received Sep. 21, 2013; accepted for publication Sep. 24, 2013; published online Oct. 15, 2013.

1 Introduction

The vital importance of the eye for living creatures is unquestionable. The part of the electromagnetic spectrum processed by the eye varies for different creatures; the human eye is sensitive to the visible spectrum for interpreting incident light and forming a clear image. A detailed anatomical description of the human eye is beyond the scope of this study. However, for the sake of completeness, we describe the main components of the eye that play crucial roles in forming images using light. Light is refracted at the front layer of the eye, called the cornea. That layer has a constant refractive index, and its contribution to refraction is almost stable over time. The only systematic age-related alteration in the cornea is that in the orientation of astigmatism, which is not considered in this paper.[1] The lens area behind the cornea has a graded refractive index (GRIN) distribution.[2,3] Two mechanisms affect the light propagation direction for the lens. The first is its curved anterior and posterior surfaces, and the second is the GRIN, which has a maximum value at the center and decays toward the edge. The lens's radii of curvature are known to decrease with time; thus, the lens becomes thicker at the center. If there is no change in the overall refractive index distribution with age, this structural alteration of the radii should make the lens more powerful, and the lens should focus incident beams in a shorter path, which is called myopia. However, the expected deterioration does not occur; this is called the lens paradox.[4,5] This phenomenon supports the claim that the refractive index distribution variation over time would compensate for myopia and maintain emmetropia.[6–8] There would be two possible variations,[9,10] either a decrement in the magnitude of the refractive index or an age-related alteration in the refractive index distribution. Research into the first idea shows that the overall refractive index magnitude does not significantly change over time.[11,12] Thus, one can infer that the refractive index distribution alters with age. This variation mechanism has been studied by many researchers. To clarify the lens paradox in this paper, we will investigate the effects of this change. There are other possible age-related changes in the refractive mechanism of the optical eye system; however, our calculations are restricted to the refractive index distribution variation.

We investigate the role of the cornea in the light-gathering process and confirm that it has greater focusing power. The accommodation of the eye ensures sharp central vision in the retina irrespective of whether the object is at a near or far point. In this paper, we investigate a single state of the accommodation of the crystalline lens. Thus, alterations in the GRIN profile due to changes in shape are not elucidated.

Modeling the human eye by a detailed analysis of the eye structure and structural parameters is of paramount importance to obtain the most accurate results. Numerous studies in the literature have contributed to an accurate model of the human eye and the GRIN profile distribution of the crystalline lens.[2,13–18] To model the eye, we have used the parameters proposed in Ref. 19.

Various types of excitation mechanisms stimulate the human body. The most abundant one is that due to visible light. Humans obtain a major portion of all their information from the environment by means of their eyes. To convert incident beams to useful

Address all correspondence to: Melih G. Can, TOBB University of Economics and Technology, Department of Electrical and Electronics Engineering, Nanophotonics Research Laboratory, Ankara 06560, Turkey. Tel: 0090 312 292 4587; Fax: 0090 312 292 4180; E-mail: m.can@etu.edu.tr

0091-3286/2013/$25.00 © 2013 SPIE

data, light should be captured by the eye cells, specifically, by rods and cones, and transmitted to the brain.[20] Visual processing is efficiently accomplished if a focused beam illuminates a region where rod and cone cells are densely located. Therefore, in this work, the age dependence of the human eye's focusing ability and aberrations are explored for various frequencies (colors) and illuminating source sizes. In this paper, we will denote the illuminating source size as the source length.

In his *Traitè de la Lumière* published in 1690, Dutch mathematician, astronomer, and physicist Christiaan Huygens discussed the propagation of light using a new principle.[21] In his book, Huygens suggested the wave theory for the first time.[22] Since then, the wave theory has been progressively developed. The wave theory of light can explain interference, diffraction, full-width at half maximum (FWHM) values, and intensity distributions, which ray optics fails to explain.[23] To date, no studies in the literature have considered modeling of the human eye and its focusing ability in terms of wave theory. Unlike previous studies, which used ray analysis in their computations, this paper investigates the optical properties of the human eye using wave analysis. The use of ray tracing is valid when the dimensions of the structure are much larger than the wavelength of the incident beam. Such an assumption is truly valid for the human eye.[23,24] However, in this work, we used wave theory to finely explore the characteristics of light propagation inside the human eye. Ray theory gives an infinitesimal spot size at the focal point. On the other hand, only wave theory analysis provides the exact FWHM value of focused light near the retina. Thus, we can measure the finite intensity value in the focal area. In addition, wave analysis provides information about the intensity of light as it traverses the layers of the eye, focuses on the back focal plane, and travels throughout the entire area of the eye.

The rest of the paper is organized as follows. In Sec. 2, we describe numerical methods of analyzing the human eye lens. We next present aberration study results and examine the roles of curved surfaces and GRIN effects in Sec. 3. The computational method uses the finite-difference time-domain (FDTD) method. Finally, Sec. 4 discusses the remarkable results presented in Sec. 3.

2 Methods

The human eye lens's focusing ability and aberrations result mainly from its curvatures and GRIN profile. To detect the individual effects and roles of these factors, we first modeled the human eye lens's anterior and posterior infinite radii while keeping the GRIN profile the same and analyzed the model under various frequencies with different source lengths. Second, we modeled the lens structure according to a configuration borrowed from the literature but kept the refractive index constant and equal to the average value.[25] We analyzed this model again for the same frequencies and source lengths. In addition, to analyze the effects of the cornea's curved structure on focusing, we modeled the cornea with various radii. Thus, the effects of the human eye's curvatures and GRIN structures on focusing and aberration are examined separately.

The structural form of the human eye will be given along with the real dimensional values. Then, the mathematical form of the refractive index distribution of the eye will be presented. A quick summary of the numerical method based on FDTD is provided along with the data handling approach.

2.1 *Structure of the Human Eye*

As we mentioned above, we deployed the eye model presented in Ref. 19. We borrowed the modeling parameters from that study; all the parameters that we used are listed for convenience in Table 1. Changes occurring in the human eye due to accommodation and aging are two different phenomena. The former involves an instantaneous response in which the shape and thickness of the eye's lens are changed via ciliary muscle contraction; this dynamic tuning ability helps produce better images. The latter, aging, induces long-term changes in the GRIN profile, lens thickness, and anterior/posterior lens surface curves. The two phenomena together assist the overall refractive power of the eye. Note that we hypothetically exclude the changes due to accommodation in our analysis.

We considered only the parts of the eye playing a significant role in focusing processes. As illustrated in Fig. 1(a), the eye has an almost spherical front surface (the cornea, the darkened part of the front surface). The focusing effect of this spherical shape of the cornea will be discussed in Sec. 3.2.

A magnified view of the crystalline lens (for an old human eye) is shown in Fig. 1(b). The GRIN profile is easily observable from the gray scale. Note that the refractive index has its maximum ($n = 1.406$) at the center of the lens and decreases toward the outer surface ($n = 1.386$). In addition to the cornea's spherical surface, the focusing effects of the GRIN profile of the crystalline lens will be discussed later in this paper.

2.2 *Human Eye Lens GRIN Profile*

The human eye lens has a distinctive refractive index distribution. Some studies describe the refractive index distribution as elliptical.[4,26–30] The curves and index distribution of the lens can be represented by many different mathematical forms. The following formula is commonly used to model the crystalline GRIN lens profile:

Table 1 Human eye model parameters borrowed from Ref. 19.

	Cornea	Lens	Cornea–Lens	Lens–Retina
Refractive index	1.376	1.406	1.336	1.337
Thickness (mm)	0.449	4.979	2.794	15.778
	Front radius (mm)		Back radius (mm)	
Cornea	7.259		8.672	
Lens	5.585		6.328	

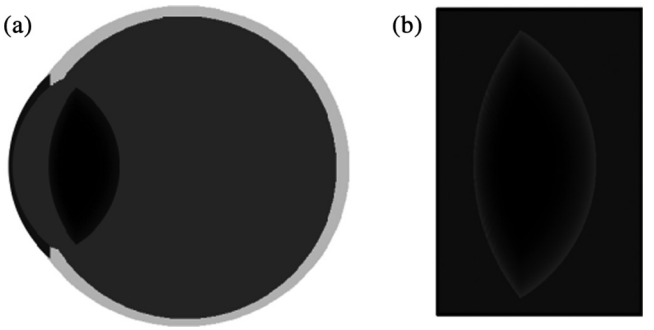

Fig. 1 Schematic view of (a) human eye structure and (b) magnified crystalline graded refractive index (GRIN) lens. The gray scale designates the refractive index variation of each section, and different layers can be distinguished from the plot.

$$n(\rho,\theta) = n_N - \Delta n\left(\frac{\rho}{\rho_s}\right)^{p(\theta)}, \quad (1)$$

where n_N is the refractive index of the lens at the center, and Δn is the index difference between the lens center and the surface. The angle θ varies along the sagittal direction from the axial direction ($\theta = 0$) to the meridional direction ($\theta = \pi/2$). Further, ρ represents the distance from the lens center ($\rho = \sqrt{x^2 + y^2}$). At an angle θ, ρ_s is the distance from the surface to the center of the crystalline lens. The power coefficient is $p(\theta = 0) = P_1$ for the axial direction and $p(\theta = \pi/2) = P_2$ for the meridional direction. Here, $p(\theta)$ represents a function of the fifth order of θ.[28]

From Eq. (1), it is clear that the refractive index of the lens varies along the sagittal axis with respect to θ and changes from the outer surface toward the central part according to the parameter ρ. For this GRIN structure, the dominant factor is the power coefficient. The steepness or smoothness of the GRIN profile is determined mainly by this parameter. In this work, the only parameter that is considered to systematically change with age is the power coefficient, as reported in Ref. 28. Consequently, we modeled human eyes with different crystalline lens profiles by using the power coefficients for young and old human eyes. The axial exponential decay P_1 is assumed to be 3, 4, and 6 for young, middle-aged, and old eyes, respectively. The respective values for the meridional exponential decay P_2 are assumed to be 2, 4, and 8.

The aim of the current work is to introduce the wave analysis concept to optical modeling of the human eye. The target is not to exploit the mathematical modeling aspect of the eye. Therefore, we selected one type of modeling extracted by optical coherence tomography even though its assumptions might be insufficient. Another formulation that describes more accurately the refractive index distribution can also be implemented well in our study by replacing Eq. (1) with the new form.

The human eye crystalline lenses and their GRIN profiles for different age intervals are illustrated in Fig. 2. With increasing age, the refractive index, which increases from the surface toward the center in both the axial and meridional directions, clearly reaches its maximum value n_N further from the center of the crystalline lens. As reported earlier, the minimum refractive index at the lens surface is stable in time, which is also the case in this work. The maximum refractive index at the cortex does not show age-related alterations.[12,29,31] It could be inferred that with aging, the maximum and minimum values of the refractive index distributions stay the same; however, the gradient profile deteriorates dramatically near the center of the lens. The calculated GRIN profiles vary in a similar manner, as reported by Jones et al.[29]

We used our new eye models in our numerical simulations based on wave theory to analyze the optical characteristics. Thus, we can observe the age dependence of the index profile of the human eye's crystalline lens, including effects such as aberrations and focal area intensity variations.

2.3 *Simulations Based on Wave Theory Analysis*

To the best of our knowledge, this is the first time that the electromagnetic wave approach is used to study the optical characteristic of the eye. We perform numerical analyses by the two-dimensional (2-D) FDTD method.[32,33] In our analyses, perfectly matched layers surrounding the entire computational window are used to serve as an absorbing boundary condition.[34] A Gaussian beam with a Gaussian amplitude profile is used as the beam source according to $E_z(y,t) = \exp[-(y - y_0)^2/\sigma_y^2]\{\exp[-(t - t_0^2)/2\Delta t^2]\}\cos(2\pi f t)$, where σ_y represents the

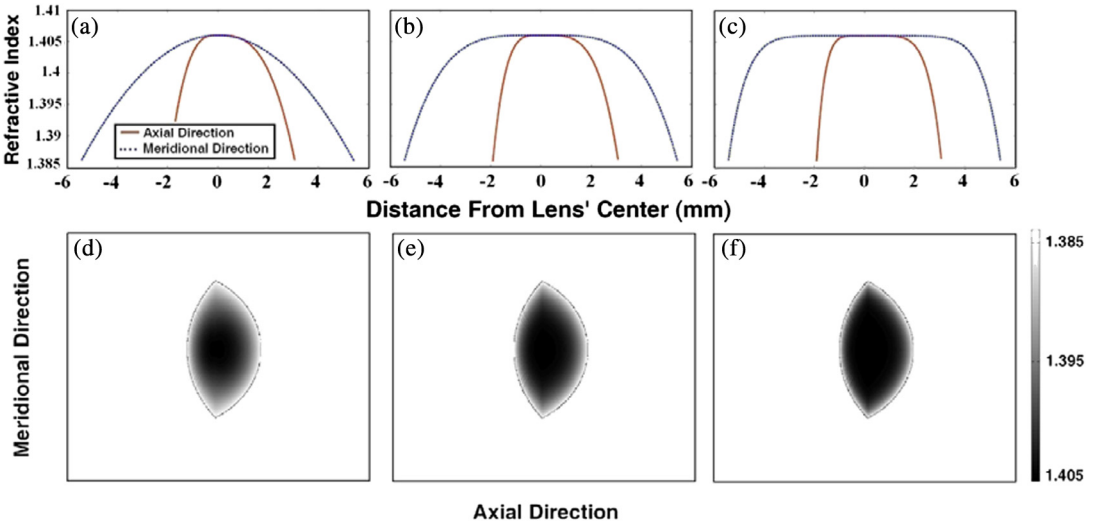

Fig. 2 GRIN profiles for (a) young, (b) middle-aged, and (c) old human lenses. Both axial and meridional directions are plotted. Crystalline lens models for (d) young, (e) middle-aged, and (f) old humans.

standard deviation of the Gaussian function. Before indicating the discretized time-domain equations, it would be useful to provide Maxwell's equations. [32]

$$\frac{\partial \vec{H}}{\partial t} = -\frac{1}{\mu}\nabla \times \vec{E}, \tag{2}$$

$$\frac{\partial \vec{E}}{\partial t} = \frac{1}{\varepsilon}\nabla \times \vec{H} - \frac{1}{\varepsilon}(\vec{J}_{\text{source}} + \sigma \vec{E}), \tag{3}$$

where $\vec{E}$ and $\vec{H}$ represent the electric and magnetic fields, respectively. The material properties of the eye are described by the permittivity ε, permeability μ, and conductivity σ. Assuming that the environment is nonmagnetic, $\mu = \mu_0$, and has zero electrical conductivity, $\sigma = 0$, the inhomogeneity of the medium is implemented via $\varepsilon = \varepsilon(x, y)$.

In a rectangular coordinate system, the transverse magnetic mode equations for the electric and magnetic fields corresponding to the above equations are given as follows:

$$\frac{\partial H_x}{\partial t} = \frac{1}{\mu}\left[-\frac{\partial E_z}{\partial y}\right], \tag{4}$$

$$\frac{\partial H_y}{\partial t} = \frac{1}{\mu}\left[-\frac{\partial E_z}{\partial x}\right], \tag{5}$$

$$\frac{\partial E_z}{\partial t} = \frac{1}{\varepsilon}\left[\frac{\partial H_x}{\partial x} - \frac{\partial H_y}{\partial y} - (J_{Z,\text{source}} + \sigma E_z)\right]. \tag{6}$$

Spatial discretization is implemented in both the temporal and spatial domains. As a result, the time and space derivative operators ∂t, ∂x, and ∂y are quantized as Δt, Δx, and Δy, respectively. We assume zero conductivity, and the eye is assumed to be made entirely of dielectric material. The term J acts as a current density. The electric and magnetic field components are updated iteratively in FDTD. The minimum spatial resolution and operating wavelength are correlated to produce correct and convergent numerical results.

Spherical aberrations occur because of the cornea's and lens's curved boundaries. In this case, we excited the eye model with sources of different lengths. All the sources were located perpendicular to the optical axis of the human eye. In addition, sources with different frequencies were used in the simulations. Therefore, we could also gather information about the chromatic aberration. To analyze the coma aberration, the source was manipulated with different nonzero incident angles.

An electromagnetic wave approach yields data that cannot be computed with ray optics. Figure 3 illustrates a single time-domain snapshot of the electric field distribution. In each case, almost 100% transmission of light is observed in the results. This is because of the small refractive index contrast ratio between the eye lens and the environment. Unlike ray optics, wave theory can be used to examine not only aberrations but also other focusing effects that vary with age in the human eye lens. The detailed results will be presented in Sec. 3.

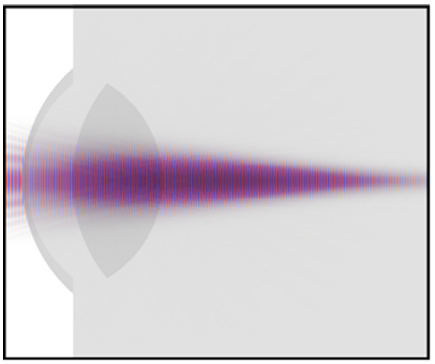

Fig. 3 Single time-domain snapshot of electric field distribution obtained by two-dimensional finite-difference time-domain method.

2.4 *Data Processing of Time-Domain Analysis*

During data processing by the FDTD method, we emphasize that the computational grid resolution with respect to the studied wavelength is an important parameter for implementing accurate analysis. When the spatial resolution is coarse, the results for the focal length yield inconsistent and erroneous values. Increasing the resolution by brute force provides more accurate data; however, because computational resources are limited, the resolution should have an upper bound. In our computations, a grid size of $\Delta x = \Delta y = \lambda/20$ is implemented as the λ-dependent mesh size, where λ is the wavelength of the incident beam. In accordance with the results obtained to find an optimum ratio, this mesh size is assumed to be the most appropriate. Dividing a wavelength into 20 segments is sufficient for accurate computation. On the other hand, using even smaller Δx and Δy values could improve the results slightly. However, simulating the model with a resolution this high is a challenging task. To find the optimum ratio, we excited our eye model with different frequency:resolution ratios while holding the other variables constant. The source size was fixed at $L = 5a$ for all frequencies, and the focal length was determined as the distance between the center of the lens and the focal position. All the sizes were determined in terms of the unit distance a, which is set to $a = 1$ mm. We realized that for all the different frequencies of light, each case has a limiting focal value that becomes saturated after we reach the optimum spatial resolution. As we mentioned above, to determine the accuracy of our approach (resolution/frequency $= 20\lambda/a$), we assumed that the tangents of the curvatures decrease exponentially. Then, we fitted exponential functions for each curvature's tangents. We neglected the tangents that remain below the 10^{-4} level; after this point, we assumed that the focal length is constant. Considering this approximation, our calculations revealed negligible error rates, such as 1.1061 and 1.1360% for the frequencies $a/\lambda = 16$ and $a/\lambda = 24$, respectively. We made a numerical evaluation of electromagnetic wave propagation through the eye using the FDTD method. However, it is well known that the size of the human eye (on the order of mm) is considerably larger than wavelengths in the visible spectrum (in the range of 300 to 700 nm). In this case, analyzing the human eye with FDTD at visible wavelengths becomes difficult because the resolution has an upper bound. The required computational power is almost impossible to supply. Hence, we performed the analysis with low frequencies. We can project the gathered data obtained from the low-frequency region to the visible spectrum.

To analyze the aberration of the human eye, we aimed to measure the focal length variation with respect to the frequency (chromatic aberration), source length (spherical aberration), and incident beam angle (coma aberration). For all these types of aberrations, we perform separate analyses of the defocusing of light along both the on- and off-axis directions.

3 Results

Here we present our results. In the Sec. 3.1, the chromatic, spherical, and coma aberrations and their results are presented with their specifications. Sec. 3.2 describes the effects of the GRIN and curvature surface on the visual process.

3.1 *Aberration Study*

To date, many studies have aimed at investigating the effect of optical aberrations in the human eye. It is important and useful to state the aberrations in functional form. Moreover, Zernike polynomials are commonly used to describe the aberrations.[23,35,36] However, in this work, we formulated the aberrations with different numerical approaches using the FDTD results. The two main effective parts associated with the aberrations are the cornea and the crystalline lens.[37,38] The surfaces and GRIN within the lens predominantly form the monochromatic aberrations. Thus, it is not unreasonable to expect that the GRIN variation with aging may change the aberrations.

We modeled the human eye structure by inserting the parameters listed in Table 1 into Eq. (1). Then we could perform our analyses based on the generated artificial structure.

3.1.1 *Chromatic aberration*

To analyze the chromatic aberrations in the young and old human eyes, we excited the eye models with sources of the same length with different frequencies. In our analyses, we worked with two different resolutions. With respect to the optimum ratio mentioned above, a minimum of 20 samples per wavelength were taken. For example, for two different normalized frequencies, 24 and 16, we have spatial resolutions of 480 and 320, respectively. When we increase the frequency, we increase the number of sampling points. Thus, we implemented a varied sampling approach.

The human eye suffers from chromatic aberration over the visible spectrum. The aberration through the axial (longitudinal) axis causes defocus between blue and red light. This characteristic of the human eye depends on the refractive index variation with wavelength, which many studies have investigated.[39–42] In these works, Cornu's hyperbolic refractive index formula is commonly used.[39,40]

$$n(\lambda) = a + \frac{b}{(\lambda - c)}, \tag{7}$$

where a, b, and c are the parameters that determine the wavelength-dependent refractive index. We can calculate the chromatic defocus by inserting Eq. (7) into the chromatic axial aberration formula.[40]

$$\Delta R = \frac{n_0 - n(\lambda)}{r(n_D)}. \tag{8}$$

In our work, we studied many different frequencies and obtained different a, b, and c values. In Eq. (8), we calculate the axial chromatic shift as ΔR. Additionally, n_0 is the reference index at a wavelength of 589 nm, and the refractive index $n_D = 1.333$. We accepted an axial defocus of zero for the reference value. This reference value and two results from our analyses are sufficient to calculate the unknown a, b, and c values. Therefore, we calculated all the a, b, and c values using our results and the reference value.

Different axial chromatic aberration results were obtained for the young and old human eye models, as shown in Figs. 4(a) and 4(b), respectively. The perpendicular dashed lines show the reference value and defocus for 589 nm. The solid lines represent the total range of the computed chromatic aberrations, and the other dashed line shows the average defocusing for each model. Note that the characteristic behavior of the presented lines in Fig. 4 is valid for the visible spectrum. The tangent value of the chromatic aberration curvature over the visible spectrum is known to decrease through the near-infrared values.[41,43] As shown in Fig. 4, we have linear chromatic aberration curves within the estimation range. Our working path is far from the visible spectrum; thus, the fitted functions may become less sensitive to the variation at the nanometer scale. The figures indicate the defocus in units of diopters (D). As shown by the defocusing illustrated in these figures, even though the axial shift in the young human eye varies in a larger region than that in the old human eye, the average defocus value is higher for the old human eye. This means that the human eye is exposed to more axial chromatic aberration as it ages. The axial chromatic aberration results for the old human eye closely resemble the results of Bedford and Wyszecki.[41] The average curves also have similar characteristics. However, their observed age range was 23 to 40, and we assume a range that extends past 60. On the other hand, they did not mention the effect of aging on chromatic aberration.

The other aberrations considered in this study are the spherical and coma aberrations. McLellan et al. proposed that higher-order monochromatic aberrations are strongly correlated with

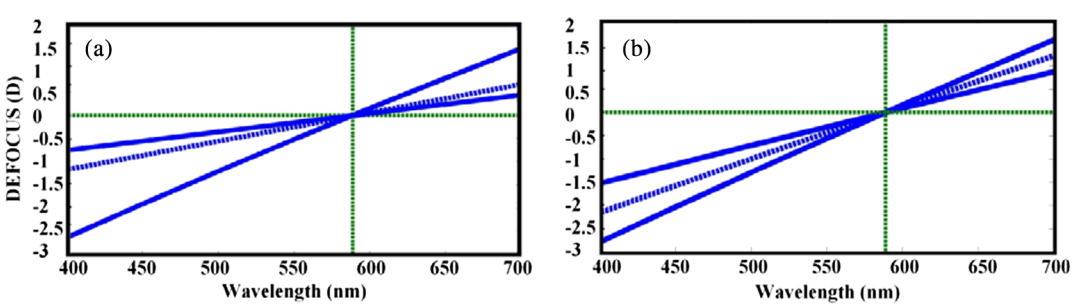

Fig. 4 Chromatic defocuses in visible spectrum for (a) young and (b) old human eyes.

age, although the lower orders may exhibit variability.[44] They investigated the root mean square wave-front error and showed a clear deterioration due to age-related coma and spherical aberrations, which will be discussed in the next section. The conclusions based on our results are consistent with the literature.

During the analyses of chromatic aberration, we inherently considered the focal length variation, whereas the frequency is the variable factor in the problem. On the other hand, we performed similar simulations while varying the source size from $5a$ to $9a$. Thus, the results show that the focal length variation depends on both the frequency and the source length. We describe the focal point–frequency variation as an indicator of chromatic aberration. Further, we can also describe the focal point–source length variation as an indicator of spherical aberration; this is presented in the next section.

3.1.2 *Spherical aberration*

An easier and efficient way of analyzing the spherical aberration of eye models is to excite the eyes using various source sizes. The focal length variation with respect to the source size is indicated in Figs. 5(a) and 5(b) for the young and old human eye models, respectively. These figures clarify the on-axis spherical aberration. They are plotted with respect to the source-size-related maximum intensity distribution on the optical axis. Thus, the focal region sizes should be investigated to explain the spherical aberration difference between young and old human eyes for a specific source size. Hence, the maximum intensity magnitude or FWHM values may enable us to detect these differences.

As seen in Figs. 5(a) and 5(b), the spherical shift characteristics of young and old human eyes differed greatly. As the source length varies from $5a$ to $6a$, the shifts in the young and old eyes are almost equal. However, even if the shift continues to vary incrementally in direction in the young eye, the spherical defocus on the longitudinal axis starts to vary in the reverse direction in the old eye after the source length exceeds $6a$. In a constant-index medium with a convex surface, the spherical shift is known to occur through the surface with increasing source length.[19,23,24] Thus, we can clearly infer that the old human eye acts as a constant-index medium when we excite it using a source size longer than $6a$. On the other hand, we cannot observe long-term characteristics of the focal defocus variations in the young human eye. Inherently, these two different defocus features are based on the eye models' different crystalline lenses. Note that the focal length is slightly smaller for the young human eye than for the old one.

One of the unique aspects of the present work is the measurement of the intensity in the focal areas. In ray analyses, the beam is focused at a point; thus, the intensity is assumed to be infinite at the focal point. However, it is well known that the intensity of the beam should be a finite and measurable quantity. The normalized intensities of the beams that we used in our spherical analyses are plotted in Fig. 6.

As expected, for both the young and old human eyes, the intensity level increases in proportion to the source length.[23,45] However, for the old eye, the normalized intensity is lower than that of the young eye. This suggests that the focusing span of the old human eye should be greater. Thus, the total range of the focused beam is larger for any source length. It is observable that age-related GRIN alteration causes an increment in the spherical aberration.

The superiority of the young human crystalline lens with respect to focusing can also be seen in Fig. 6. The deviations in the intensity value between the focal areas of the young and old human eyes arise from differences in focusing capability. Note that better imaging requires fine focusing. Thus, it can be deduced that young eyes perform imaging better than old eyes. In addition, the intensity value depends on the transmission efficiency of the light. As illustrated in Fig. 2, the young human eye lens has a more pronounced GRIN profile than the old one; hence, the young human eye can exhibit less reflection loss and a strong focusing power.

We simulated different models with many different parameters and excited these structures with various frequencies and source lengths. However, for all the cases described so far, we located the source perpendicular and symmetric to the optical axis. To analyze the coma aberration, we used tilted Gaussian sources with different incident angles. For this aberration type, the computations are performed only for the young human eye. We aimed to observe the effects of the tilted sources. Tabernero et al. proposed that the tilted human eye lens may compensate for the coma.[46] The outcome of the coma aberration study is presented in the next section.

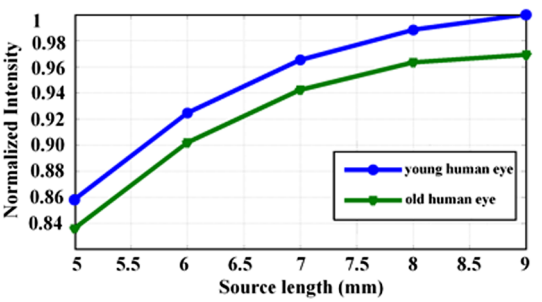

Fig. 6 Normalized intensity variations depending on source lengths for young and old human eyes.

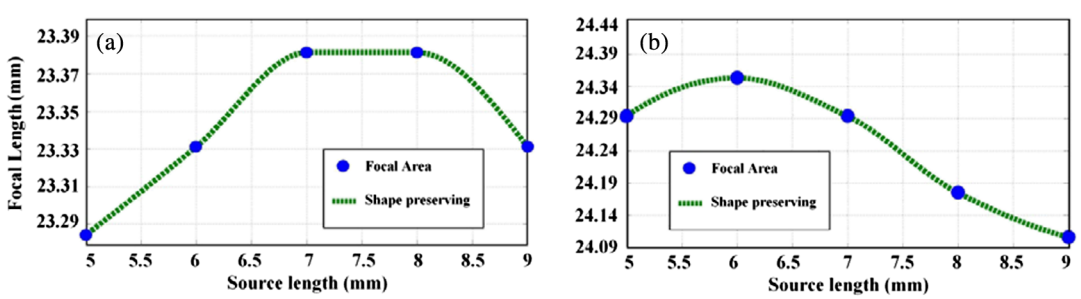

Fig. 5 Focal length versus source length for (a) young and (b) old human eyes.

3.1.3 *Coma aberration*

In any type of imaging lens, different types of aberration occur. One type is coma aberration. Coma aberration occurs because of variations in the incident angle of light. To analyze the effects of coma aberration, we illuminated the structure with light at increasing incident angles. The source size is fixed at $10a$, and the frequency is fixed at $a/\lambda = 5$. We used a spatial resolution of 100 and fixed the parameter σ_y in the Gaussian beam formula. We excited the eye with light at incident angles of 0, ± 5, ± 10, ± 15, and ± 20 deg with respect to the optical axis. Significant variation is observed when the angle of incidence is changed. Under zero incident angle (perpendicular excitation), the light is focused almost on the retina. On the other hand, if the incident angle changes, the focal points move away from the retina. In addition, the intensity on the retina decreases as we send an oblique source. Table 2 summarizes these observations. Note that the intensity corresponding to perpendicular excitation is taken as the reference (maximum intensity), and the other cases are normalized with respect to that value.

θ_{inc} and θ_{ref} correspond to the incident and refraction angles, respectively. The ΔR values in Table 2 correspond to the distance between the focal point and the retina for each incident angle. The normalized intensity variation is denoted as ΔI_{norm}.

The two remarkable consequences of oblique excitation are an alteration in the focal point and an intensity reduction. For example, when the incident angle is 20 deg, the focal point is $\sim$1.2 mm from the front surface of the retina. The intensity drops sharply to less than half of the maximum value.

The amount of light impinging on the retina is shown in polar coordinates in Fig. 7. The intensity values are not normalized in this case. As expected, a symmetric dependency appears for positive and negative excitation angles. In addition, this intensity distribution is similar to the photoreceptor and nerve fiber distributions of the human eye.[47] The cone cell and nerve fiber distributions have a peak value on the fovea, and we see that their density decreases when we investigate the retina outside of the fovea. The nerve fibers terminate in a small area; however, the cone cell density continuously decreases. On the other hand, on the fovea, there are almost no rod cells. The rod cell density increases greatly outside of the fovea, and on a considerable part of the retina, it is higher than the cone cell density. One of the most intriguing implications of this observation is the similarity between the nerve fiber density distribution and the intensity distribution that we plotted in Fig. 7.

Table 2 Incident and refraction angles with respect to the optical axis and corresponding distances between focal point and retina. The last column shows normalized intensity variations.

θ_{inc} (deg)	θ_{ref} (deg)	ΔR (mm)	ΔI_{norm}
0	0	0.1512	1
5	3.4323	0.3884	0.7616
10	6.8792	0.6360	0.6557
15	10.0913	0.8690	0.5270
20	13.6424	1.2016	0.4078

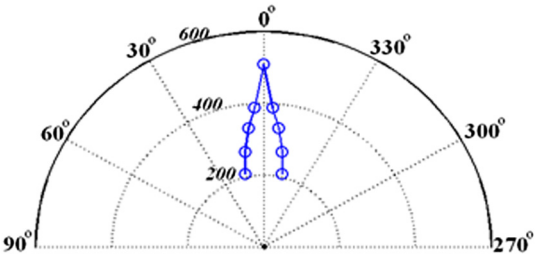

Fig. 7 Polar plot of angle-related intensity variation on the retina.

The spatial and spectral resolution of imaging is proportional to the amount of light incident on the retina. Therefore, it is crucial to quantify how the focusing element (the human eye in this study) performs under oblique excitation.

In our research, we focused on the advantages of using the electromagnetic wave approach. One of these advantages is the ability to measure the FWHM values at the focal point. It is desirable that the focal regions be located on the retina's surface. Figure 8 shows a snapshot from the computational window that we used during the FDTD analyses.

The light distribution over the eye is presented on top of the structure. We observe strong light focusing on the retina and negligible back-reflection from the curved interfaces. The solid arc in the backplane of the eye represents the location of the retina. The cross-section of the intensity profile along the dashed line is plotted in Fig. 8(b). The line crosses over the central point of the retina on the optical axis. As shown in Fig. 8(b), the normalized intensity reaches its maximum value at the center of the retina. The incident angle is zero, and the light source is symmetric with respect to the optical axis. The illustration shows that the focal point appears where the optical axis (black spotted region) and the retina intersect. The transverse profile of the light shows a peak value and very weak low side lobes. The distance between the focal point and the retina is small. The beam does not spread while propagating such a short distance. The FWHM value is $\sim 2\lambda$. In the visible spectrum, this FWHM value corresponds to $\sim 1\ \mu m^2$ spot size considering the circular geometry of the problem.

Figure 9 shows superimposed time-domain snapshots of three different incident angle beams. The snapshots were taken while each beam was focused near the retina. As indicated in Fig. 9, the incident angles are 10, 0, and -20 deg. The focal point of the beam clearly appears further from the retina as the incident angle deviates from normal incidence. In the time-domain snapshots, the intensity distribution is indicated by a color bar. In the figure, the focal areas have higher intensity values. With increasing incident angle, the intensity reaching the retina becomes smaller. It is also apparent that the maximum intensity values at the focal spans decrease with increasing incident angle. Because the same optical system and source type are used, this phenomenon clarifies that the aberrations due to coma extend the focal span in the propagation direction.

3.2 *Curvature Surface and GRIN Effects*

The role of curvature surfaces and GRIN effects in the visual process is an important question. We hypothetically modeled three eye structure types for young and old human eyes to analyze the effect of the curvature on focusing. The modeled structures are depicted in Fig. 10.

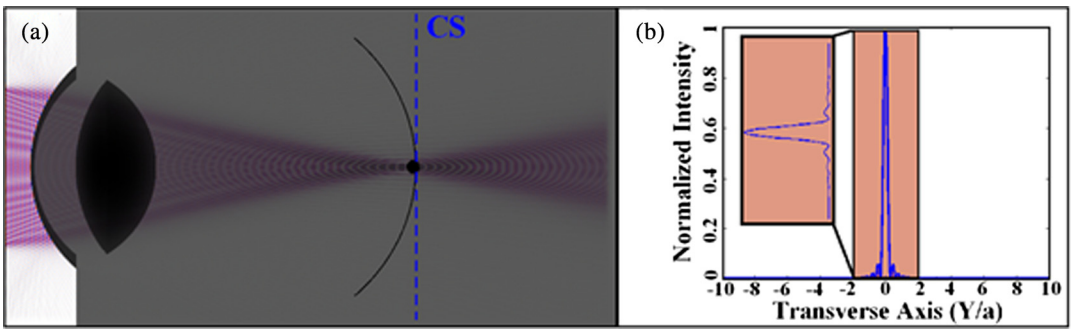

Fig. 8 Time-domain snapshots of (a) light distribution and (b) normalized intensity profile along the cross-section of the central retina (on the optical axis) through the transverse axis. Inset shows magnified view of shaded region.

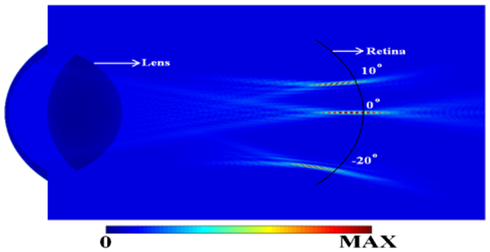

Fig. 9 Intensity profiles of focused beams with different incident angles. Schematic views of the eye shape and the location of the retina are superimposed on the light distribution.

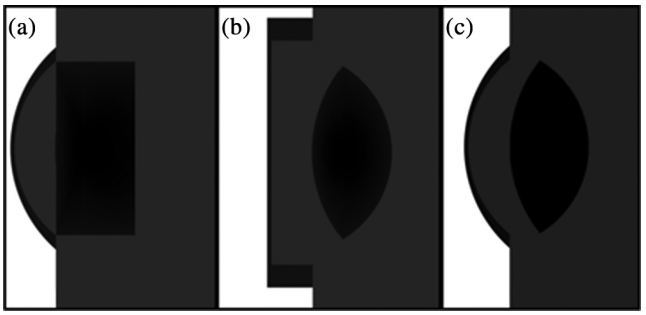

Fig. 10 Three human eye models with (a) rectangle GRIN lens and curved cornea, (b) flat cornea and curved GRIN lens, (c) constant (averaged) refractive index lens with curved interfaces.

First, we model the human eye lens as a rectangle [Fig. 10(a)]. The width is equal to the maximum width of the crystalline lens, and the height is equal to the maximum height of the eye lens. We modeled this new rectangular lens with a GRIN profile expressed by Eq. (1). In the second and third models, the human eye is configured with a cornea of infinite radius [Fig. 10(b)] and with a constant refractive index lens with curved surfaces [Fig. 10(c)], respectively. Thus, the effects of the cornea's curved structure and the lens's curvature and GRIN profile on focusing are independently modeled, simulated, and investigated.

We obtained intriguing focal length variations with the manipulated human eye model. In light of the results, we can discuss the effects of the curvature and GRIN profile on focusing; we can also classify the regions of the human eye according to their effects on focusing. Table 3 presents the focal length variations. It indicates the percentage of the focal length difference between the manipulated models and the human eyes modeled in accordance with Tables 1 and 2 and Eq. (1).

Table 3 Focal length variations [as percentages compared to models using Tables 1 and 2 and Eq. (1)] for rectangular GRIN lens, flat cornea, and constant (average) refractive index.

Human eye	Rectangular GRIN	Flat cornea	Constant index
Young (%)	16.9	127.7	12
Old (%)	14.3	135.0	6.8

On the basis of the results in Table 3, we can emphasize two conclusions. First, the most significant variation for both young and old human eyes occurs when the cornea is manipulated. Second, the young human eye is much more sensitive to lens variations than the old human eye. The majority of the light-focusing power is due mainly to the curved front and back surfaces of the human eye. This configuration corresponds to Fig. 10(b).

4 Discussion and Conclusion

In this work, the age dependence of the focusing properties of the human eye is systematically illustrated. The frequency, source size, GRIN variation in the crystalline lens of the eye, and curved shape of the cornea are shown to remarkably affect the focal length and focusing power of the eye. Note that the only age-related variation is assumed to be that in the GRIN distribution. Thus, this study is limited in this respect. The importance of the study includes new way of electromagnetic wave analysis for a given eye model and insights obtained for light propagation inside the human eye.

We verified the ray analysis results for the human eye by performing electromagnetic wave theory analysis. Moreover, measurements that can be computed only by wave analysis were made for eyes of different ages. All the results are compatible with the literature. For specific source sizes and frequencies, the focal length takes its maximum value when the propagation direction is parallel to the optical axis. However, deviations in the incident angle shorten the focal length. Focusing away from the retina increases scattering and causes larger halos on the retina. This widening increases the spot size of the beam, and the enlarged spot sizes of many beams could interfere on the retina. Interference of the beams increases the blurriness of the image.

The GRIN structure of the eye is one of the main topics of this work. We show the human eye GRIN profile in Fig. 2. A significant difference between an adolescent and an old human eye lens is the flatness of the refractive index profile. An old lens is almost homogeneous except at the surface. However, a young lens reaches its maximum refractive index smoothly at the center. During propagation in an old human eye, the refracted beam reaches the maximum index faster than in the young human eye because of the flat index region in the old eye's GRIN profile. Equation (9), known as the Eikonal equation, represents the mathematical expression of this case,

$$\frac{d}{ds}\left(n\frac{d\vec{r}}{ds}\right) = \vec{\nabla} n, \tag{9}$$

where n represents the refractive index, $ds = \sqrt{dx^2 + dy^2}$, and $\vec{dr}$ is the vector representation of the light propagation direction.[48] According to this expression, the propagating beam bends toward the high-index region. If the index does not vary, the beam propagates along a straight path. Thus, with respect to the difference between the GRIN profiles of old and young human eyes, one can infer that the light is diffracted more in the young human eye lens. The beam focuses earlier than in the old human eye lens. Therefore, the intensity of the focused light is higher in the young human eye than in the old human eye.[45] As proposed in Ref. 10, the propagation direction, formed mainly by the lens surfaces and the GRIN, has a minor effect on refraction. Thus, we may conclude that Table 3 is compatible with the literature.

As we mentioned above, we used Ref. 19 for the eye model in this paper. For our model, Fig. 5 indicates that the distance from the cornea's front surface to the focal area varies between 23.29 and 23.39 mm for the young human eye and between 24.09 and 24.35 mm for the old human eye. Hence, we can state that the focal length shifts with age. We can also cite the shift in focal length as a possible reason for the visual impairment that occurs with aging. These types of visual defects are treated with convex lens glasses. To investigate the relation between the surface and the focusing properties, we first considered the effects of the spherical shape of the cornea and the crystalline lens. The variation in the lens curvature affects the old eye less than the young eye. Similarly, a constant-index eye lens shifts the focal length of the young human eye lens almost twice as much as that of the old human eye. In contrast, the cornea curvature affects an old eye more. Hence, we can infer that the GRIN profile of the old human eye lens enables the lens to compensate more for lens and GRIN deformations. Thus, with increasing age, a healthy cornea structure becomes more critical.

Note that for the old lens, the focal length varies between the homogeneous and the young lens values. This variation arises from the steep variation in the GRIN profile of the old human eye lens. The index distribution in the old human eye lens does not vary obviously near the lens center; the only variation can be observed near the surfaces. This type of variation causes the old human eye lens to act like a constant refractive index lens.

In our analyses, we conclude that the cornea has a larger effect than the crystalline lens on the focusing ability because of the small gradient of the lens. For both old and young eyes, variations in the cornea change the focusing properties considerably, as also reported in Ref. 49. One of the most significant results that we obtained by our analyses is that the intensity variation over the retina is very similar to the nerve fiber distribution. We can speculate that the nerve fiber evolution may be based on the intensity distribution on the retina. The fibers may grow in proportion to the intensity in the early stages of their evolution.

Aging dramatically deforms the human eye lens's GRIN profile. As a result, the human eye suffers from aberrations. According to our findings, the old human eye's average chromatic axial defocus is almost twice that of the young human eye, and the spherical shift variation range of the old eye is almost three times that of the young eye. This suggests that accommodation requires greater effort as the eye ages. Moreover, the intensity at the focal area decreases with age. Ultimately, even if the structure of the eye is undamaged, the eye loses its visual ability with age.

Finally, the ability to analyze the human eye using the electromagnetic wave approach may pave the way to exploring other significant concepts related to eye research. For example, laser surgery employs either continuous or pulsed sources.[49] One can deeply investigate the interaction of high-energy light sources with the types of material in the eye.

Acknowledgments

The authors gratefully acknowledge the financial support of the Scientific and Technological Research Council of Turkey (TUBITAK), project number 110T306. H.K. also acknowledges partial support from the Turkish Academy of Sciences.

References

1. B. K. Pierscionek, "Aging changes in the optical elements of the eye," *J. Biomed. Opt.* **1**(2), 147–156 (1996).
2. S. Nakao et al., "Model of refractive indices in the human crystalline lens," *Jpn. J. Clin. Ophthalmol.* **23**, 903–906 (1969).
3. D. A. Palmer and J. Sivak, "Crystalline lens dispersion," *JOSA* **71**(6), 780–782 (1981).
4. H. Saunders, "Age dependence of human refractive errors," *Ophthalmic Physiol. Opt.* **1**(3), 159–174 (1981).
5. G. Smith and B. K. Pierscionek, "The optical structure of the lens and its contribution to the refractive status of the eye," *Ophthalmic Physiol. Opt.* **18**(1), 21–29 (1998).
6. B. K. Pierscionek, "Presbyopia–effect of refractive index," *Clin. Exp. Optom.* **73**(1), 23–30 (1990).
7. G. Smith, D. A. Atchison, and B. K. Pierscionek, "Modeling the power of the aging human eye," *JOSA A* **9**(12), 2111–2117 (1992).
8. J. F. Koretz and C. A. Cook, "Presbyopia and visual homeostasis: compensatory aging mechanisms," in *Vision Science and Its Applications*, pp. 106–109, Optical Society of America (1999).
9. J. F. Koretz and G. H. Handelman, "How the human eye focuses," *Sci. Am.* **259**(1), 92–99 (1988).
10. B. K. Pierscionek and J. W. Regini, "The gradient index lens of the eye: an opto-biological synchrony," *Prog. Retinal Eye Res.* **31**(4), 332–349 (2012).
11. B. K. Pierscionek et al., "Nondestructive method of constructing three-dimensional gradient index models for crystalline lenses: I. Theory and experiment," *Am. J. Optom. Physiol. Opt.* **65**(6), 481 (1988).
12. B. K. Pierscionek and D. Y. Chan, "Refractive index gradient of human lenses," *Optom. Vis. Sci.* **66**(12), 822–829 (1989).
13. A. C. Kooijman, "Light distribution on the retina of a wide-angle theoretical eye," *JOSA* **73**(11), 1544–1550 (1983).
14. W. Sródka, "Biomechanical model of human eyeball and its applications," *Opt. Appl.* **39**(2), 401–413 (2009).
15. O. Pomerantzeff, P. Dufault, and R. Goldstein, "Wide-angle optical model of the eye," in *Advances in Diagnostic Visual Optics*, G. M. Breinin and I. M. Siegel, Eds., pp. 12–21, Springer-Verlag, Berlin (1983).

16. O. Pomerantzeff et al., "Wide-angle optical model of the eye," *Am. J. Optom. Physiol. Opt.* **61**(3), 166–176 (1984).
17. R. Montalbán et al., "Intrasubject repeatability of corneal morphology measurements obtained with a new Scheimpflug photography-based system," *J. Cataract Refract. Surg.* **38**(6), 971–977 (2012).
18. R. A. Schachar, "Central surface curvatures of postmortem-extracted intact human crystalline lenses: implications for understanding the mechanism of accommodation," *Ophthalmology* **111**(9), 1699–1704 (2004).
19. E. Hecht, *Optics*, 2nd ed., Addison-Wesley, Reading, Massachusetts (1987).
20. C. Oyster, Ed., "Retina I: photoreceptors and functional organization," Chapter 13 in *The Human Eye: Structure and Function*, pp 545–594, Sinauer Associates, Sunderland, Massachusetts (1999).
21. C. Huygens, *Treatise on Light*, Tredition Classics, Hamburg-Germany (2012).
22. C. W. Biligs and J. Tabak, *Lasers: The Technology and Uses of Crafted Light*, Facts on File, New York, NY (2006).
23. M. Born and E. Wolf, *Principles of Optics*, 4th. ed., Pergamon Press, London (1970).
24. M. C. Teich and B. E. Saleh, *Fundamentals of Photonics*, Vol. 22, Wiley, New York (1991).
25. S. R. Uhlhorn et al., "Refractive index measurement of the isolated crystalline lens using optical coherence tomography," *Vis. Res.* **48**(27), 2732–2738 (2008).
26. B. Patnaik, "A photographic study of accommodative mechanisms: changes in the lens nucleus during accommodation," *Investig. Ophthalmol. Vis. Sci.* **6**(6), 601–611 (1967).
27. J. Blaker, "Toward an adaptive model of the human eye," *J. Opt. Soc. Am.* **70**(2), 220–223 (1980).
28. A. de Castro et al., "Three-dimensional reconstruction of the crystalline lens gradient index distribution from OCT imaging," *Opt. Express* **18**(21), 21905–21917 (2010).
29. C. E. Jones et al., "Refractive index distribution and optical properties of the isolated human lens measured using magnetic resonance imaging (MRI)," *Vis. Res.* **45**(18), 2352–2366 (2005).
30. W. Drexler, "Ultrahigh-resolution optical coherence tomography," *J. Biomed. Opt.* **9**(1), 47–74 (2004).
31. B. K. Pierscionek, "Refractive index contours in the human lens," *Exp. Eye Res.* **64**(6), 887–893 (1997).
32. A. Taflove and S. C. Hagness, *Computational Electrodynamics: The Finite-Difference Time-Domain Method*, Artech House Publisher, Norwood, MA (2005).
33. F. Oskooi et al., "MEEP: a flexible free software package for electromagnetic simulations by the FDTD method," *Comput. Phys. Commun.* **181**(3), 687–702 (2010).
34. J. P. Berenger, "A perfectly matched layer for the absorption of electromagnetic waves," *J. Comput. Phys.* **114**(2), 185–200 (1994).
35. A. S. C. Felix et al., "Comparison of refractive power maps from a reference surface: geometric versus Zernike power polynomials," *Proc. SPIE* **8499**, 849907 (2012).
36. A. Gargallo, J. Arines, and E. Acosta, "Lens aberrations and their relationship with lens sutures for species with Y-suture branches," *J. Biomed. Opt.* **18**(2), 025003 (2013).
37. P. Artal and A. Guirao, "Contributions of the cornea and the lens to the aberrations of the human eye," *Opt. Lett.* **23**(21), 1713–1715 (1998).
38. P. Artal et al., "Compensation of corneal aberrations by the internal optics in the human eye," *J. Vis.* **1**(1), 1–8 (2001).
39. L. N. Thibos et al., "The chromatic eye: a new reduced-eye model of ocular chromatic aberration in humans," *Appl. Opt.* **31**(19), 3594–3600 (1992).
40. E. J. Fernández et al., "Ocular aberrations as a function of wavelength in the near infrared measured with a femtosecond laser," *Opt. Express* **13**(2), 400–409 (2005).
41. R. E. Bedford and G. Wyszecki, "Axial chromatic aberration of the human eye," *J. Opt. Soc. Am.* **47**(6), 564–565 (1957).
42. F. W. Campbell and R. W. Gubisch, "Optical quality of the human eye," *J. Physiol.* **186**(3), 558–578 (1966).
43. G. Wald and D. R. Griffin, "The change in refractive power of the human eye in dim and bright light," *JOSA* **37**(5), 321–334 (1947).
44. J. S. McLellan, S. Marcos, and S. A. Burns, "Age-related changes in monochromatic wave aberrations of the human eye," *Investig. Ophthalmol. Vis. Sci.* **42**(6), 1390–1395 (2001).
45. A. Yariv and Y. Pochi, *Photonics: Optical Electronics in Modern Communications (The Oxford Series in Electrical and Computer Engineering)*, 6th ed., Chapter 2.6, Oxford University Press Inc., New York, NY (2006).
46. J. Tabernero et al., "Mechanism of compensation of aberrations in the human eye," *JOSA* **24**(10), 3274–3283 (2007).
47. H. Gross, F. Blechinger, and B. Achtner, "Human eye," Chapter 36 in *Handbook of Optical Systems*, H. Gross, Ed., Vol. 4, pp. 1–87, Wiley-VCh, Weinheim (2008).
48. C. Gomez-Reino, M. V. Perez, and C. Bao, *Gradient-Index Optics: Fundamentals and Applications*, Springer, Berlin (2002).
49. S. Dua, U. R. Acharya, and E. Y. K. Ng, *Computational Analysis of the Human Eye with Applications*, World Scientific Publishing Company Incorporated, Singapore (2011).